

## Article

# Flexible Humidity Sensor Based on Au Nanoparticles/Organosilica-Containing Polyelectrolyte Composite

Pi-Guey Su \*  and Chih-Chang Hsu

Department of Chemistry, Chinese Culture University, Taipei 111, Taiwan; asd87524773@gmail.com

\* Correspondence: spg@ulive.pccu.edu.tw; Tel.: +886-2-28610511 (ext. 25332)

**Abstract:** A novel flexible humidity sensor incorporating gold nanoparticles (Au NPs) and a tri-functional organosilica compound has been developed through the integration of sol-gel processing, free radical polymerization, and self-assembly techniques. The trifunctional organosilica was initially synthesized by modifying (3-mercaptopropyl)trimethoxysilane (thiol-MPTMS) with 3-(trimethoxysilyl)propyl methacrylate (vinyl-TMSPMA). Subsequently, a hydrophilic polyelectrolyte, [3(methacryloylamino)propyl]trimethyl ammonium chloride (MAPTAC), was grafted onto the MPTMS-TMSPMA gel. The Au NPs were assembled onto the thiol groups present in the MPTMS-TMSPMA-MAPTAC gel network. The compositional and microstructural properties of the Au NPs/MPTMS-TMSPMA-MAPTAC composite film were investigated utilizing Fourier transform infrared spectroscopy (FTIR) and scanning electron microscopy (SEM). The presence of thiol groups and mesoporous silica skeletons ensured the stability of the humidity-sensing film on the substrate under highly humid conditions, while the hydrophilic groups functioned as humidity-sensitive sites. This innovative humidity sensor demonstrated high sensitivity, acceptable linearity, minimal hysteresis, and rapid response time across a broad range of working humidity levels. Based on the complex impedance spectra analysis, hydronium ions ( $\text{H}_3\text{O}^+$ ) were determined to govern the conductance process of the flexible humidity sensor.

**Keywords:** flexible humidity sensor; organosilica; Au NPs; composite; water resistance



**Citation:** Su, P.-G.; Hsu, C.-C.

Flexible Humidity Sensor Based on Au Nanoparticles/Organosilica-Containing Polyelectrolyte Composite. *Chemosensors* **2023**, *11*, 291. <https://doi.org/10.3390/chemosensors11050291>

Academic Editor: Marco Frasconi

Received: 16 April 2023

Revised: 3 May 2023

Accepted: 11 May 2023

Published: 13 May 2023



**Copyright:** © 2023 by the authors. Licensee MDPI, Basel, Switzerland. This article is an open access article distributed under the terms and conditions of the Creative Commons Attribution (CC BY) license (<https://creativecommons.org/licenses/by/4.0/>).

## 1. Introduction

Fabricating flexible sensors has emerged as a critical area of interest, particularly in the context of portable handheld consumer electronics, which are utilized in applications such as smart textiles, smart packaging, radio frequency identification (RFID) tags, and the Internet of Things (IoT) [1–4]. The measurement and control of humidity is necessary in maintaining the excellent quality of products in a variety of manufacturing processes, as well as in maintaining human health and performing daily activities. Therefore, humidity sensors have attracted much attention and have found wide use in various fields such as industrial process control, agriculture, health monitoring, and environmental monitoring [5–7]. Consequently, the development of flexible humidity sensors and wearable devices has gained significant traction [8–10]. To achieve high accuracy and precision in flexible humidity sensors that cater to the diverse needs of various applications, it is imperative to enhance the properties of humidity-sensing films in terms of cost efficiency, ease of fabrication, sensitivity, hysteresis, linearity, mechanical stability, response/recovery times, and working range [7,11,12]. As a result, an array of materials including polymers [13–19], carbon-based nanomaterials [20–26], ceramic materials [27–29], and diverse composite materials [30–38] has been employed in flexible humidity-sensing films. In comparison to polymers, ceramics demonstrate superior sensitivity, rapid response/recovery times, and enhanced stability under high humidity conditions.

Mesoporous silica has garnered considerable interest for humidity sensor applications due to its exceptional properties such as non-toxicity, high internal specific surface area, and

ordered pores [39–42]. However, a lack of sufficient hydrophilic groups and low conductivity restricts its humidity-sensing capabilities across a wide humidity range. To enhance the hydrophilic properties of silica materials, a common method involves modifying them with polymer electrolytes, as these exhibit significant conductivity changes when exposed to varying relative humidity (RH) environments [43–47]. Various researchers have developed resistive and capacitive-type humidity sensors using different materials and methods, such as in situ polymerization and thiol–ene click reactions [43–47]. Additionally, incorporating materials such as Au nanoparticles (Au NPs), single-walled carbon nanotubes (SWCNTs), or graphene oxide (GO) into silica has been used to improve conductivity and flexibility, thereby enhancing humidity-sensing properties [11,48–50]. In a previous study [11], a flexible humidity sensor comprising Au nanoparticles, GO, and silica was fabricated using a sol–gel process and a self-assembly technique. However, there have been no attempts to utilize organosilica-containing polyelectrolyte-based materials in the fabrication of a flexible humidity sensor. In this study, Au NPs/organosilica-containing polyelectrolyte ((3-mercaptopropyl)trimethoxysilane (MPTMS)-3-(trimethoxysilyl)propyl methacrylate (TMSP-MA)-[3(methacryloylamino)propyl]trimethyl ammonium chloride (MAPTAC) (MPTMS-TMSPMA-MAPTAC) composite films were fabricated on a polyethylene terephthalate (PET) substrate to create flexible resistive-type humidity sensors by combining sol–gel processing, free radical polymerization, and self-assembly. Fourier transform infrared spectroscopy (FTIR) and scanning electron microscopy (SEM) were used to analyze the composition and morphologies of the Au NPs/MPTMS-TMSPMA-MAPTAC composites. The electrical characteristics of the Au NPs/MPTMS-TMSPMA-MAPTAC composite films were investigated as functions of RH. The water resistance, flexibility, and humidity-sensing properties encompassing sensitivity, hysteresis, influence of ambient temperature, effect of applied frequency, response/recovery times, and stability were also examined. The humidity-sensing mechanism of the Au NPs/MPTMS-TMSPMA-MAPTAC composite film was studied by using complex impedance spectra.

## 2. Experimental Methods

### 2.1. Materials

Tetraethoxysilane (TEOS, 99%, Sigma-Aldrich, St. Louis, MO, USA), (3-mercaptopropyl) trimethoxysilane (MPTMS, 95%, Sigma-Aldrich, St. Louis, MO, USA), 3-(trimethoxysilyl)propyl methacrylate (TMSPMA, 98%, Sigma-Aldrich, St. Louis, MO, USA), [3(methacryloylamino)propyl] trimethyl ammonium chloride (MAPTAC, 50%, Sigma-Aldrich, St. Louis, MO, USA), ethanol (95%, Sigma-Aldrich, St. Louis, MO, USA), hydrochloric acid (0.1 mol/L, Sigma-Aldrich), sodium citrate (99%, Sigma-Aldrich, St. Louis, MO, USA) and hydrogen tetrachloroaurate(III) hydrate ( $\text{HAuCl}_4 \cdot x\text{H}_2\text{O}$ , 99.9%, Sigma-Aldrich, St. Louis, MO, USA) were purchased. All the used deionized water (DIW) was prepared using a Milli-Q Millipore (Bedford, MA, USA) purification system.

### 2.2. Fabrication of Au NPs

The Au NPs were synthesized following the procedure described in our previous publication [11]. The colloidal Au NPs were prepared by incorporating 38.8 mM sodium citrate into 1 mM  $\text{HAuCl}_4$  aqueous solution, heated to boiling, and maintained at this temperature for 15 min with continuous vigorous stirring. Subsequently, the mixture was allowed to cool to room temperature and stored at 4 °C prior to utilization.

### 2.3. Fabrication of Flexible Humidity Sensor Based on Au NPs/MPTMS-TMSPMA-MAPTAC Composite

Figure 1 provides a schematic representation of the flexible humidity sensor structure. Interdigitated Au electrodes on a flexible PET substrate were fabricated by initially sputtering Cr (50 nm of thickness) followed by Au (250 nm of thickness) at 120 °C. The gap of electrode measured 0.25 mm. Figure 2 illustrates the fabrication process of a flexible resistance-type humidity sensor employing sol–gel processing, free radical polymerization,

and self-assembly. Initially, 0.56 M MPTMS and 0.56 M TMSPMA were dissolved in 60 mL of 0.1 M HCl and ethanol solution (0.065 mole) under stirring at room temperature using a one-pot method. Subsequently, 0.08 M MAPTAC and 0.01 g AIBN were introduced into the as-prepared TMSPMA-MPTMS sol solution, and the mixture was heated at 70 °C for 24 h with continuous stirring. The resulting MPTMS-TMSPMA-MAPTAC sol-gel solution was then deposited onto a PET substrate and dried at 60 °C for 4 h. Finally, the MPTMS-TMSPMA-MAPTAC sol-gel was immersed in an Au NPs solution for 5 h at 4 °C, yielding a flexible resistive-type humidity sensor. In comparison to the organosilica-based material, a pristine SiO<sub>2</sub> film was also synthesized via the hydrolysis of TEOS.

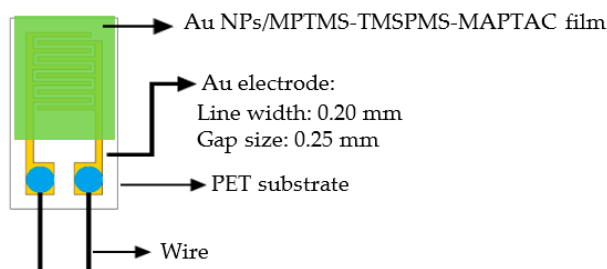


Figure 1. Schematic diagram of flexible humidity sensor.

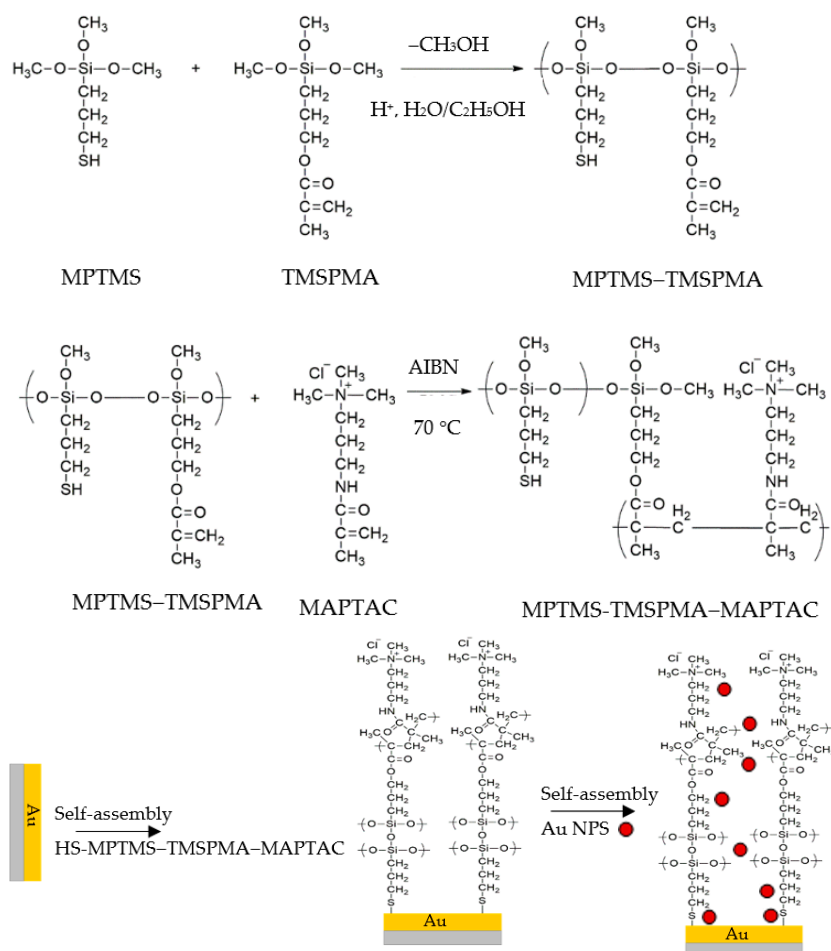
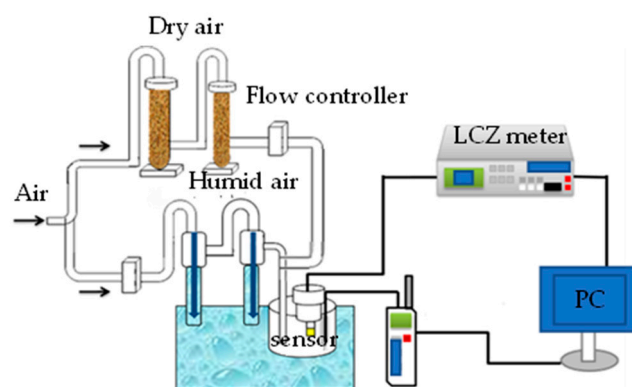


Figure 2. Fabrication of a flexible humidity sensor based on Au NPs/MPTMS-TMSPMA-MAPTAC film by combining the sol-gel process, free radical polymerization, and self-assembly method.

## 2.4. Instruments and Analysis

The infrared (IR) spectra of the MPTMS, MPTMS-TMSPMA, and MPTMS-TMSPMA-MAPTAC films were studied using a Fourier transform infrared spectrometer (Nicolet 380). The surface microstructures of the pristine SiO<sub>2</sub>, MPTMS-TMSPMA-MAPTAC, and Au NPs/MPTMS-TMSPMA-MAPTAC composite films coated onto PET substrates were studied by using a scanning electron microscope (SEM, TM 4000, Hitachi, Ibaraki, Japan). Figure 3 illustrates the humidity sensor measurement system within a temperature-controlled chamber. A divided humidity generator system was employed to produce the required test humidity conditions by adjusting the proportion of dry and humid air under a total flow rate of 10 L/min. The required RH values were determined using a standard humidity hygrometer (with an accuracy of  $\pm 0.1\%$  RH). An LCZ meter was utilized to measure the impedance values of the flexible humidity sensors as a function of RH. The maximum humidity atmosphere (97% RH) for water-resistance testing was controlled by a saturated K<sub>2</sub>SO<sub>4</sub> solution. The measurement conditions for complex impedance analysis were set at an applied frequency range of 50 Hz to 100 kHz, an applied voltage of 1 V, and a humidity range from 20 to 90% RH at 25 °C.



**Figure 3.** Schematic plots of the humidity atmosphere controller system and impedance measurement of flexible humidity sensors.

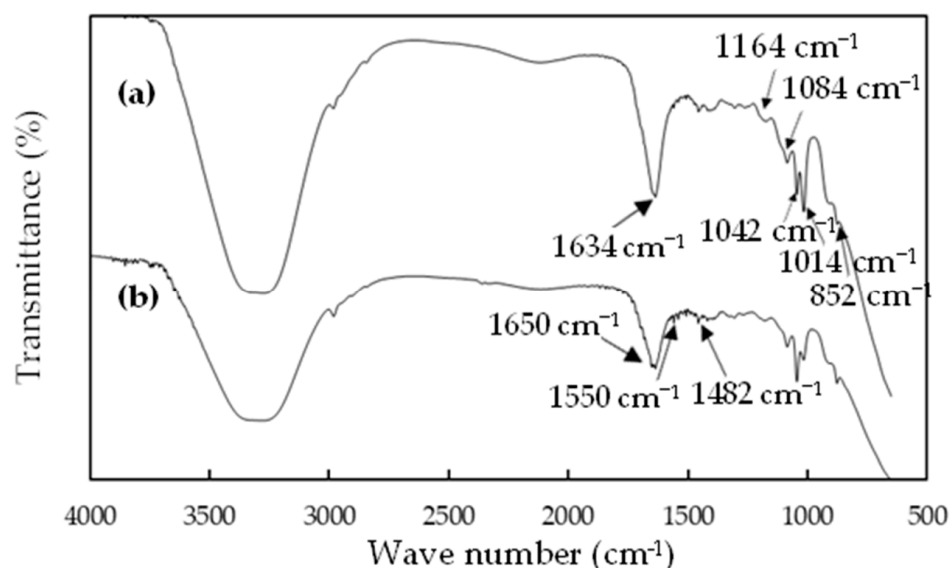
## 3. Results

### 3.1. Preparation and Characterization of Au NPs/MPTMS-TMSPMA-MAPTAC Composite

Figure 2 illustrates the fabrication process of a flexible resistive-type humidity sensor composed of the Au NPs/MPTMS-TMSPMA-MAPTAC composite film. Initially, thiol-containing organosilica (thiol-MPTMS) functionalized with vinyl-containing organosilica (TMSPMA-vinyl) was synthesized using a hydrolyzed sol-gel process via crosslinkable silanol groups. Subsequently, a hydrophilic organic unit (MAPTAC) was chemically modified onto the thiol-MPTMS-TMSPMA-vinyl utilizing a free radical polymerization method. Additionally, some methoxy groups are still present on the final network, but certainly not one per monomer. Finally, the Au NPs were incorporated into the MPTMS-TMSPMA-MAPTAC using self-assembly. The as-prepared MPTMS-TMSPMA sol includes trifunctional groups, namely the vinyl head group, the siloxane middle group, and the thiol tail group. The vinyl head groups can be chemically modified with hydrophilic MAPTAC, generating a strong force to bind the host and guest materials together, thus enhancing the response of the MPTMS-TMSPMA-MAPTAC film to humidity. The siloxane middle groups form a three-dimensional (3D) network, not only providing stereo sites for Au NPs attachment, but also improving stability in high humidity environments. The thiol tail groups serve a dual purpose: they can chemisorb onto the Au electrode surface and participate in the assembly of the Au NPs by forming Au-S bonds, ultimately enhancing the adhesion strength on the PET substrate, and improving the stability of the flexible sensors. Self-assembling Au NPs on the organosilica gel offers conduction paths that enhance the conductivity of the MPTMS-TMSPMA-MAPTAC film.

### 3.1.1. IR Analysis

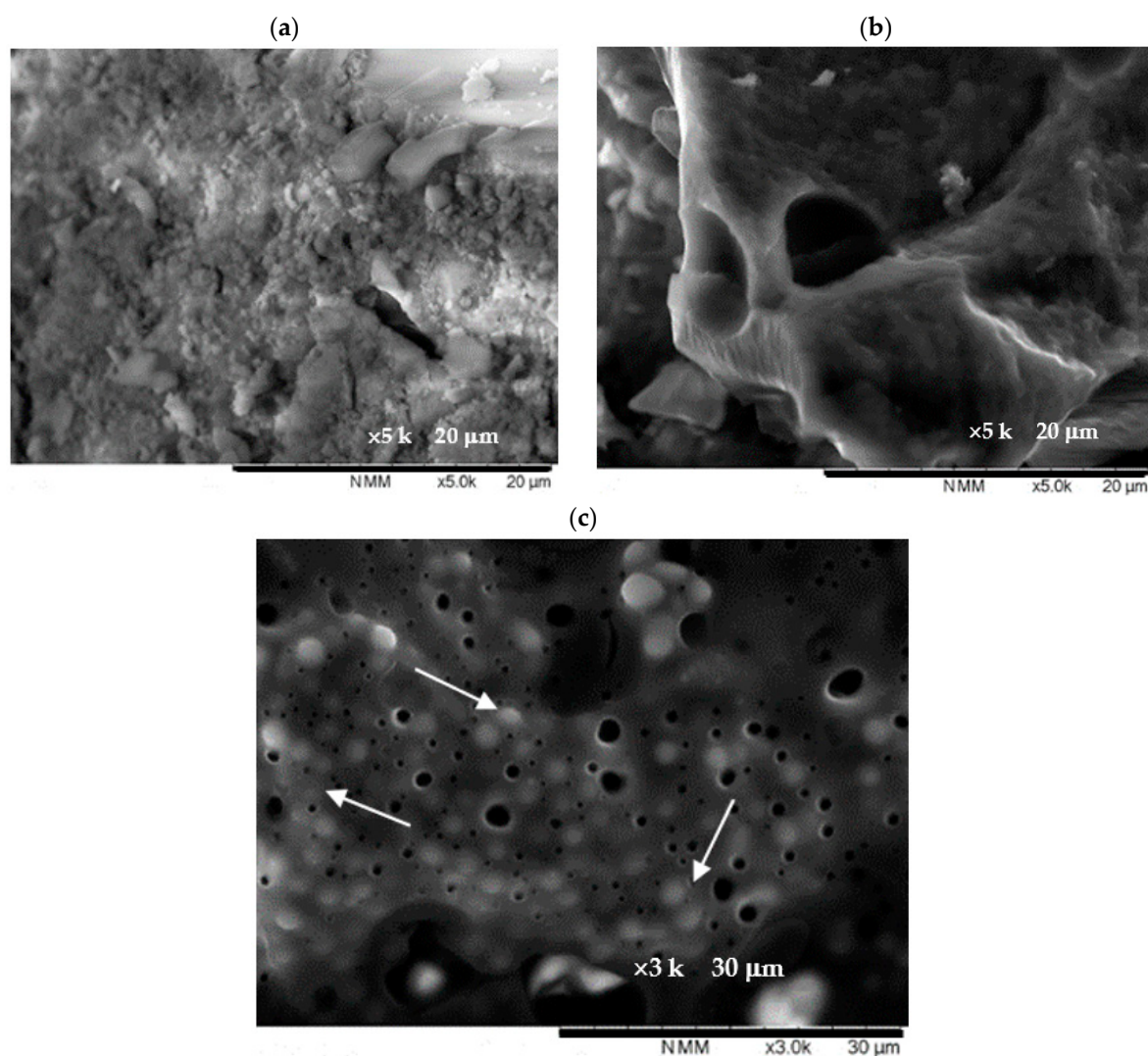
Figure 4a,b display the FT-IR spectra of the as-prepared MPTMS-TMSPMA and MPTMS-TMSPMA-MAPTAC sol-gel, respectively. The peak appearing at  $852\text{ cm}^{-1}$  indicates the presence of the stretching of -C-S- group in the MPTMS structure. Two peaks emerging at  $1014$  and  $1042\text{ cm}^{-1}$  correspond to the stretching vibrations of the cross-linked -Si-O-Si- framework. The peaks at  $1084$  and  $1164\text{ cm}^{-1}$  signify the respective stretching of O-C-C and C-C-O of the ester groups in the TMSPMA structure. Another crucial band of TMSPMA is confirmed at  $1634\text{ cm}^{-1}$ , attributed to the mixture of stretching vibrations of C=O and C=C groups [51]. These results verify that the vinyl-containing organosilica (TMSPMA-vinyl) was successfully functionalized with thiol-containing organosilica (thiol-MPTMS). Regarding the IR spectrum of MPTMS-TMSPMA-MAPTAC (Figure 4b), the characteristic peaks at  $1650$  and  $1542\text{ cm}^{-1}$  correspond to the C=ONH and CON-H groups, respectively, in the MAPTAC structure. Additionally, the IR spectrum of MPTMS-TMSPMA-MAPTAC exhibits the same primary characteristic absorption peaks of MPTMS-TMSPMA in the  $1200\text{--}800\text{ cm}^{-1}$  range. These results suggest that MAPTAC was successfully incorporated into the MPTMS-TMSPMA sol-gel.



**Figure 4.** IR spectra of (a) MPTMS-TMSPMA and (b) MPTMS-TMSPMA-MAPTAC sol-gel.

### 3.1.2. SEM Analyses

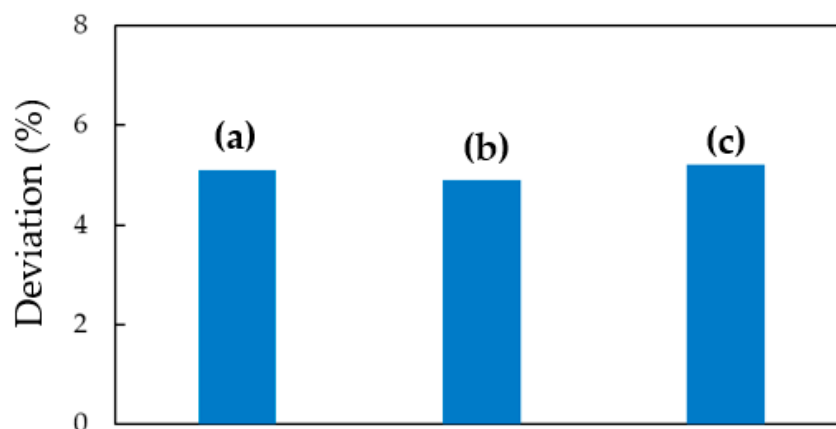
Figure 5 displays the SEM images of the pristine  $\text{SiO}_2$ , MPTMS-TMSPMA-MAPTAC, and Au NPs/MAPTAC-TMSPMA-MPTMS composite films. Figure 5a reveals that the pristine  $\text{SiO}_2$  film exhibits a fractured and cracked surface, which can result in instability of the flexible properties. In contrast, the SEM of the MPTMS-TMSPMA-MAPTAC film (Figure 5b) demonstrates a much smoother surface with numerous pores on the film's surface. This is because the organosilica tends to produce more organic sites homogeneously branched to the pore walls, which better supports the film's cohesion on a PET substrate. Compared to the MPTMS-TMSPMA-MAPTAC film, the Au NPs/MAPTAC-TMSPMA-MPTMS composite film (Figure 5c) indicates that the Au NPs are embedded within the MPTMS-TMSPMA-MAPTAC matrix with no uncovered areas present on its surface. Moreover, the Au NPs were randomly embedded into the composite film. The aggregation of the Au NPs was observed. This phenomenon can be attributed to the thiol-containing organosilica gel providing stereo sites for anchoring the Au NPs.



**Figure 5.** SEM images of (a) pristine  $\text{SiO}_2$  film, (b) MPTMS-TMSPMA-MAPTAC film and (c) Au NPs/MPTMS-TMSPMA-MAPTAC composite film. (White arrows indicate the Au NPs.)

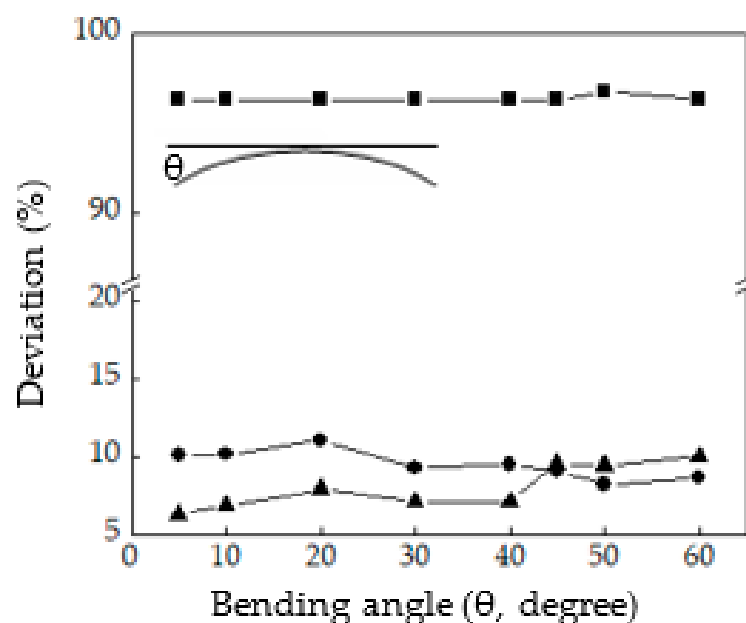
### 3.2. Water-Resistance and Flexibility Properties of Au NPs/MPTMS-TMSPMA-MAPTAC Composite Film

Figure 6 illustrates the deviation of flexible humidity sensors based on pristine  $\text{SiO}_2$ , MPTMS-TMSPMA-MAPTAC, and Au NPs/MPTMS-TMSPMA-MAPTAC composite films after being placed in a highly humid (97% RH) environment for 5 days. The deviation was determined by using the formula  $(\log Z_{60\% \text{ RH}} - \log Z'_{60\% \text{ RH}}) / \log Z_{60\% \text{ RH}} \times 100\%$ , where  $\log Z_{60\% \text{ RH}}$  and  $\log Z'_{60\% \text{ RH}}$  represent the impedance values of the flexible humidity sensors at 60% RH before and after the sensor was placed in the high humidity atmosphere (97% RH), respectively. In comparison to the pristine  $\text{SiO}_2$  film, no noticeable deviation was observed for the MPTMS-TMSPMA-MAPTAC and the Au NPs/MPTMS-TMSPMA-MAPTAC composite films, indicating good water resistance due to the silica skeletons ensuring stability in high humidity environments. Furthermore, the thiol-containing MPTMS-TMSPMA-MAPTAC film can be anchored onto a gold electrode, thus improving the stability of the sensing film in high humidity environments. Additionally, the incorporation of Au NPs did not reduce the water resistance of the Au NPs/MPTMS-TMSPMA-MAPTAC composite film.



**Figure 6.** Water resistance of (a) pristine SiO<sub>2</sub> film, (b) MPTMS-TMSPMA-MAPTAC film and (c) Au NPs/MPTMS-TMSPMA-MAPTAC composite film on high humidity, measured at 1 V, 1 kHz and 25 °C.

Figure 7 depicts the flexibility of humidity sensors based on pristine SiO<sub>2</sub>, MPTMS-TMSPMA-MAPTAC, and Au NPs/MPTMS-TMSPMA-MAPTAC composite films. At each bending angle, the sensor was exposed to 60% RH. The deviation of the impedance of the flexible humidity sensors was determined by using the formula  $(\log Z_{60\% RH, f} - \log Z_{60\% RH, b}) / \log Z_{60\% RH, f} \times 100\%$ , where  $\log Z_{60\% RH, f}$  and  $\log Z_{60\% RH, b}$  represent the impedance of the flat and bent flexible humidity sensor at 60% RH, respectively. The deviation of the pristine SiO<sub>2</sub> film reached up to 96% even at an angle of 5° due to its rigid nature. In contrast, both the MPTMS-TMSPMA-MAPTAC and Au NPs/MPTMS-TMSPMA-MAPTAC composite films exhibited strong flexibility at angles of up to 60°, with deviations within 10%. This outcome can be attributed to their soft organosilica skeleton structure.



**Figure 7.** Flexibility of ■: pristine SiO<sub>2</sub> film, ▲: MPTMS-TMSPMA-MAPTAC film and ●: Au NPs/MPTMS-TMSPMA-MAPTAC composite film on PET substrate, measured at 1 V, 1 kHz and 25 °C.

### 3.3. Electrical and Humidity-Sensing Properties of Au NPs/MPTMS-TMSPMA-MAPTAC Composite Film

Figure 8 displays the log-impedance of the pristine SiO<sub>2</sub>, MPTMS-TMSPMA, MPTMS-TMSPMA-MAPTAC, and Au NPs/MPTMS-TMSPMA-MAPTAC composite films as a

function of RH. Table 1 summarizes the results of the sensitivities and linearities of the linear fitting curve. The pristine  $\text{SiO}_2$  film had only a small change in impedance with humidity over the studied range (20% to 90% RH) due to its insulating nature. The MPTMS-TMSPMA film displayed only a small change in impedance with humidity over the studied range (20% to 90% RH) because more crosslinkable silicol groups were modified onto the MPTMS-TMSPMA film, resulting in hydrophobic and low-conductance properties. The impedance of the MPTMS-TMSPMA-MAPTAC film decreased over a wider range of RH (20% to 90% RH) than the MPTMS-TMSPMA film, because the highly hydrophilic organic compound (MAPTAC) was chemically modified onto TMSPMA-MPTMS, thus improving its sensitivity. The impedance of the Au NPs/MPTMS-TMSPMA-MAPTAC film decreased more than that of the MPTMS-TMSPMA-MAPTAC film with humidity over the studied range (20% to 90% RH), indicating that the Au NPs were anchored into MPTMS-TMSPMA-MAPTAC, consequently generating a new conductive pathway and enhancing the conductivity of this material. The flexible humidity sensor composed of the Au NPs/MPTMS-TMSPMA-MAPTAC composite film had the greatest sensitivity ( $0.0533 \log Z/\%RH$ ), good linearity ( $R^2 = 0.9562$ ) (Table 1), the greatest flexibility (less 10% at an angle of up to  $60^\circ$ ), and good stability in a high-humidity environment. Accordingly, its humidity-sensing properties were further studied.

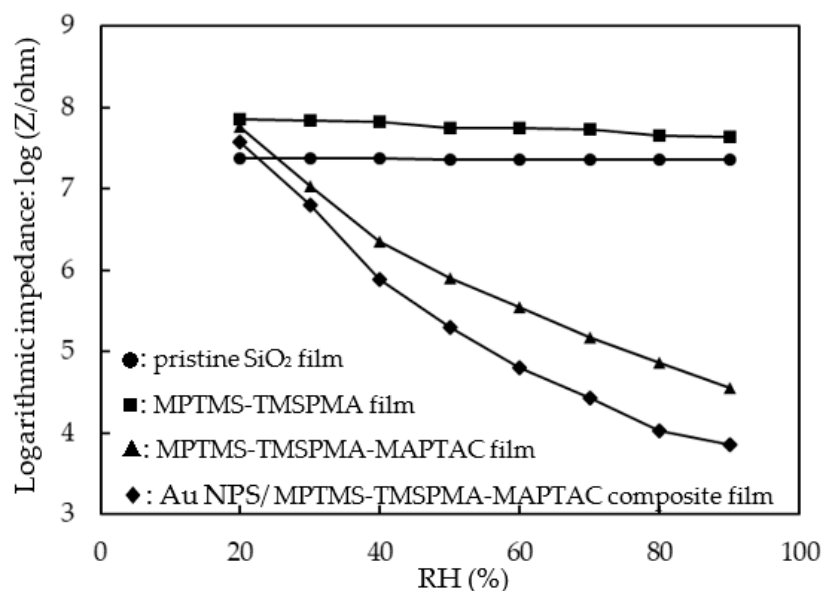


**Figure 8.** Impedance versus RH for flexible humidity sensors based on pristine  $\text{SiO}_2$ , MPTMS-TMSPMA, MPTMS-TMSPMA-MAPTAC and Au NPs/MPTMS-TMSPMA-MAPTAC composite films, measured at 1 V, 1 kHz and  $25^\circ\text{C}$ .

**Table 1.** Sensitivity and linearity of flexible humidity sensors based on pristine  $\text{SiO}_2$ , MPTMS-TMSPMA, MPTMS-TMSPMA-MAPTAC and Au NPs/MPTMS-TMSPMA-MAPTAC composite films.

Materials	Sensing Curve	
	Sensitivity ( $\log Z/\%RH$ ) <sup>a</sup>	Linearity ( $R^2$ ) <sup>b</sup>
Pristine $\text{SiO}_2$	-0.0003	0.9646
MPTMS-TMSPMA	-0.0034	0.9609
MPTMS-TMSPMA-MAPTAC	-0.0442	0.9694
Au NPs/MPTMS-TMSPMA-MAPTAC	-0.0533	0.9562

<sup>a</sup> Sensitivity was defined as the slope of the logarithmic impedance versus RH plot in the range from 20 to 90% RH. <sup>b</sup> Linearity was shown as the correlation coefficient of the logarithmic impedance versus RH plot in the range from 20 to 90% RH.

Figure 9a illustrates the hysteresis phenomenon observed in the flexible humidity sensing device. The mean hysteresis remained within a 3.5% relative humidity (RH) margin throughout a dehydration-to-humidification cycle, which encompassed the complete spectrum of relative humidity, ranging from 20% to 90% RH. In Figure 9b, the influence of the surrounding temperature on the  $\log Z$  for the flexible humidity sensor as a function of RH is depicted. The temperature coefficient was approximately  $-0.55\% \text{ RH}/^\circ\text{C}$  for temperatures between 15 and 35  $^\circ\text{C}$ , spanning a humidity range from 20% to 90% RH. Additionally, as the temperature increases from 25  $^\circ\text{C}$  to 35  $^\circ\text{C}$ , the impedance of the flexible humidity slightly changed over the studied range (20% to 90% RH). This phenomenon was related to the fact that the intermediate backbone was inorganic silicon, resulting in the vibration generated by the increase in temperature being slight, so the impedance drop was not obvious. Figure 9c presents the consequences of varying the applied frequency on the  $\log Z$  for the flexible humidity sensor as a function of RH. Impedance measurements were conducted at frequencies of 1, 5, 11, and 100 kHz with an applied voltage of 1 V. A distinct decline in the impedance of the flexible humidity sensor was observed below 40% RH as the applied frequency escalated. The curve representing the  $\log Z$  versus RH exhibited the highest degree of humidity-sensing linearity at a frequency of 1 kHz. Figure 9d illustrates the response and recovery times for the flexible humidity sensor, assessed at a temperature of 25  $^\circ\text{C}$  and a frequency of 1 kHz. The response time ( $T_{res.90\%}$ ) and recovery time ( $T_{rec.90\%}$ ) are characterized as the durations necessary for the impedance of the flexible humidity sensor to undergo a 90% shift in its maximal variation, following humidification and desiccation processes ranging from 10% to 90% RH and 90% to 10% RH, respectively.  $T_{res.90\%}$  and  $T_{rec.90\%}$  were determined to be 15 s and 100 s, respectively. Figure 9e displays the long-term stability of the flexible humidity sensor. No significant deviation in the  $\log Z$  for the flexible humidity sensor was detected over a 29-day period at the examined RH values of 20%, 60%, and 90% RH. Table 2 juxtaposes the humidity-sensing characteristics of the current flexible humidity sensor with those of sensors documented in prior reports [43–47]. In comparison to organosilica-based materials, such as SBA-15 [45,46] and MCM-41 [47], the fabricated flexible humidity sensor, which utilizes an Au NPs/MPTMS-TMSPMA-MAPTAC composite film, demonstrated superior flexibility, commendable water resistance, and a comparable response time and hysteresis.

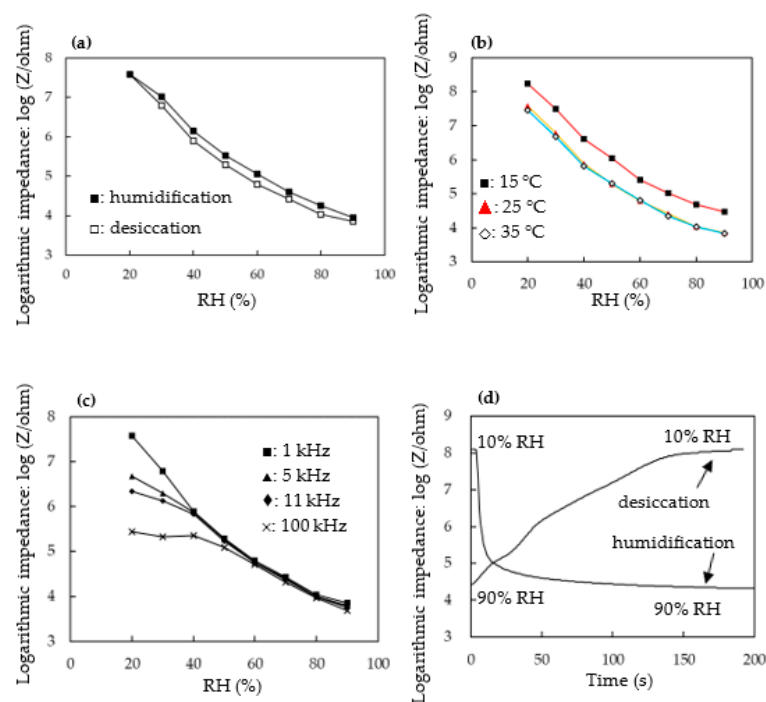
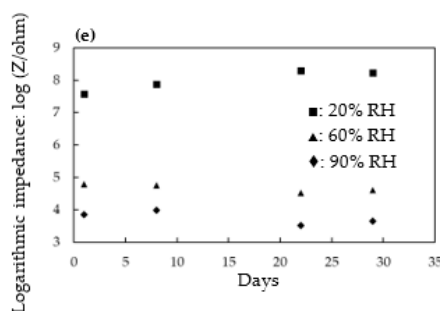


Figure 9. Cont.



**Figure 9.** Humidity-sensing properties of the flexible humidity sensor based on the Au NPs/ MPTMS-TMSPMA-MAPTAC composite film. (a) Hysteresis of the sensor, (b) effect of ambient temperature, (c) effect of applied frequency, (d) response/recovery times, (e) long-term stability.

**Table 2.** Comparison of performance of flexible humidity sensor developed herein with the literature based on organicsilica materials and their composites.

Sensing Material	Working Range (%RH)	Sensitivity $-(\log Z/\% \text{ RH})$	Hysteresis (% RH)	Flexibility (%) (log Z Deviation)	Response Time (s)	References
SiO <sub>2</sub> -poly-AMPS	30–90	0.0571	2%	-	-	[43]
APTOS <sup>a</sup> /n-butyl bromide	11–97	-	1%	-	13	[44]
SBA-15/MATMAC <sup>b</sup>	11–95	-	2%	-	11	[45]
SBA-15/sodium p-styrenesulfonate	11–95	-	-	-	5	[46]
MCM-41/PEDOT	11–95	-	6	-	165	[47]
Au NPs/MPTMS-TMSPMA-MAPTAC	20–90	0.0533	3.5%	<10%	15	This work

<sup>a</sup> APTOS: 3-aminopropyltriethoxysilane. <sup>b</sup> MATMAC: methacrylateethyl trimethyl ammonium chloride.

### 3.4. Humidity-Sensing Mechanism

Impedance spectroscopy is a powerful method to investigate the conduction mechanisms of humidity sensors. Therefore, impedance spectroscopy is employed to explicate the ion transport as the humidity-sensing mechanism for the flexible humidity sensor, which is made of an Au NPs/MPTMS-TMSPMA-MAPTAC composite film. Figure 10 exhibits the complex impedance spectra for the flexible humidity sensor across an RH range from 30% to 90% RH. The impedance evaluations were performed at frequencies between 50 Hz and 100 kHz, an alternating current (AC) voltage of 1 V, and a temperature of 25 °C. The horizontal axis ( $Z_r$ ) represents real component of the impedance ( $Z$ ), while the vertical axis ( $Z_i$ ) shows the imaginary component of  $Z$ . At a low RH of 30% (Figure 10a), a discernible semicircular curve was observed, primarily attributable to the intrinsic impedance of the film. As the RH increased to 40% (Figure 10b), a distorted and diminishing semicircle at elevated frequencies became evident. This suggests that some of the physisorbed water molecules on the Au NPs/MPTMS-TMSPMA-MAPTAC composite film started to gradually dissociate, forming  $\text{H}_3\text{O}^+$  ions, resulting in diffusing from the humidity-sensing film to the Au electrode. At a high RH of 90% (Figure 10c), only a straight line is apparent, indicating the  $\text{H}_3\text{O}^+$  ions predominate the conductance process within the Au NPs/MPTMS-TMSPMA-MAPTAC composite film. An equivalent circuit of such complex impedance plots is shown in Figure 10d. At low relative humidity, the semicircle was modeled as an equivalent circuit of parallel association of resistor ( $R_f$ ) and capacitor ( $C_f$ ). At high relative humidity, the complex impedance plot was modeled as an equivalent circuit of the serial association of resistor ( $R_f$ ) and the impedance at the electrode/sensing film (Warburg impedance,  $Z_w$ ), which was caused by the diffusion of  $\text{H}_3\text{O}^+$  ions across the interface between the electrode and the humidity-sensing film. Finally, the sorbed water acted as a plasticizer, increasing the mobility of the solvated  $\text{H}_3\text{O}^+$  ions, which dominated the conduction in the sensor. Therefore, according to the obtained complex impedance spectra, the  $\text{H}_3\text{O}^+$  ions are the dominant factor influencing the conduction characteristics of

the flexible humidity sensor based on the Au NPs/MPTMS-TMSPMA-MAPTAC composite film [52,53].

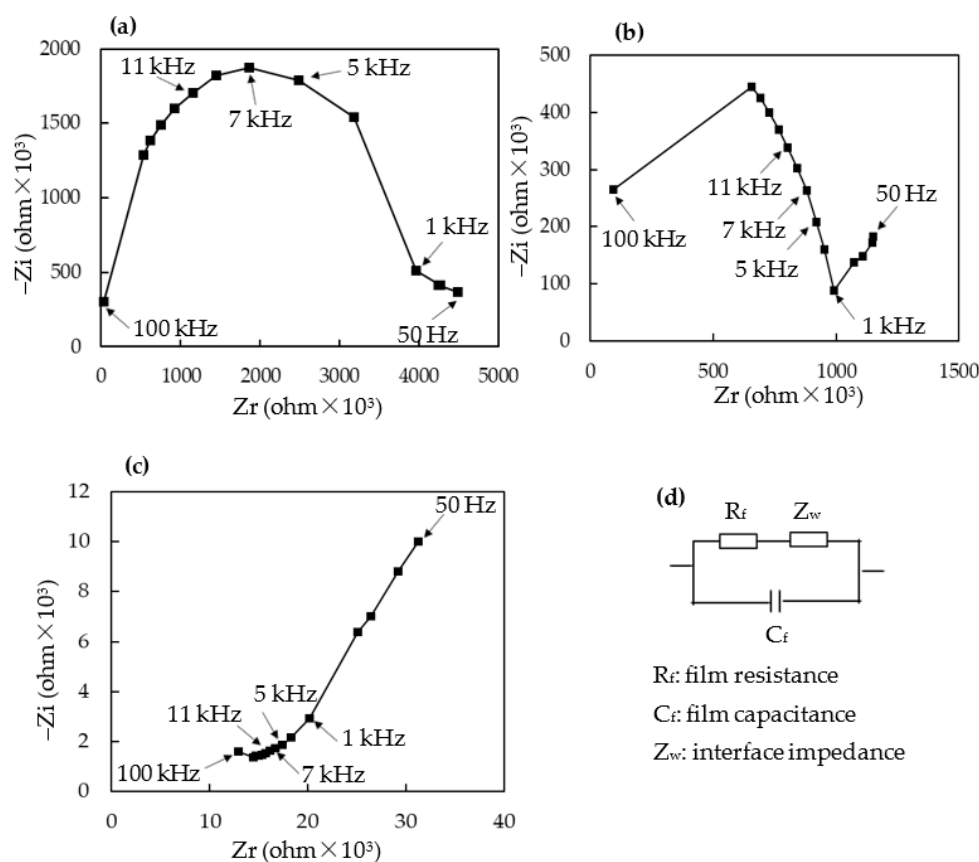


**Figure 10.** Complex impedance plots of the flexible humidity sensor based on Au NPs/MPTMS-TMSPMA-MAPTAC composite film at (a) 30% RH, (b) 40% RH (c) 90% RH. (d) Equivalent circuit of the flexible humidity sensor.

#### 4. Conclusions

A novel flexible impedance-based humidity sensor utilizing an Au NPs/MPTMS-TMSPMA-MAPTAC composite film was engineered by integrating sol-gel processing, free radical polymerization, and self-assembly techniques. Thiol groups and mesoporous silica skeletons can be anchored to the Au electrode, creating a three-dimensional network that offers stereo sites for the attachment of Au NPs, thereby enhancing the stability of the humidity-sensing film in high-humidity environments. The hydrophilic organic units, MAPTAC, underwent chemical modification on the mesoporous organosilica, augmenting the sensitivity of humidity sensing. Furthermore, the self-assembled Au NPs supplied conduction pathways, ameliorating the conductivity of the humidity-sensing film, and consequently improving its sensitivity. The flexible humidity sensor, composed of the Au NPs/MPTMS-TMSPMA-MAPTAC composite film, displayed excellent water resistance, superior sensitivity, and satisfactory linearity ( $Y = -0.0533X + 8.2654$ ;  $R^2 = 0.9562$ ) between the  $\log Z$  and the RH range from 20% to 90% RH. Additionally, it exhibited low hysteresis (less 3.5% RH) and a small temperature coefficient ( $-0.55\% \text{ RH}/^\circ\text{C}$ ). Analysis of the complex impedance spectra for this flexible humidity sensor, which utilized the Au NPs/MPTMS-TMSPMA-MAPTAC composite film, revealed a transition from a semicircular curve at 30% RH to a straight line at 90% RH. This observation underscores the dominant role of  $\text{H}_3\text{O}^+$  ions in governing the conductivity variations within this humidity sensor.

**Author Contributions:** Conceptualization, P.-G.S.; Methodology, P.-G.S. and C.-C.H.; Investigation, P.-G.S. and C.-C.H.; Writing—original draft preparation, P.-G.S. and C.-C.H.; Writing—review and editing, P.-G.S.; Supervision, P.-G.S.; Project administration, P.-G.S.; Funding acquisition, P.-G.S. All authors have read and agreed to the published version of the manuscript.

**Funding:** This research was funded by National Science and Technology Council of Taiwan, grant no. MOST 111-2113-M-034-001.

**Data Availability Statement:** Not applicable.

**Conflicts of Interest:** The authors declare no conflict of interest.

## References

1. Cochrane, C.; Hertleer, C.; Schwarz-Pfeiffer, A. *Smart Textiles in Health: An Overview, in Smart Textiles and Their Applications*; Koncar, V., Ed.; Woodhead Publishing: Sawston, UK, 2016; Volume 178, pp. 9–32.
2. Wasson, T.; Choudhury, T.; Sharma, S.; Kumar, P. Integration of RFID and sensor in agriculture using IOT. In Proceedings of the International Conference on Smart Technologies for Smart Nation (SmartTechCon), Bengaluru, India, 17–19 August 2017; pp. 217–222.
3. Mezzanotte, P.; Palazzi, V.; Alimenti, F.; Roselli, L. Innovative RFID sensors for Internet of Things applications. *IEEE J. Microw.* **2021**, *1*, 55–65. [[CrossRef](#)]
4. Zuo, J.; Feng, J.; Gameiro, M.G.; Tian, Y.; Liang, J.; Wang, Y.; Ding, J.; He, Q. RFID-based sensing in smart packaging for food applications: A review. *Future Foods* **2022**, *6*, 100198. [[CrossRef](#)]
5. Amin, E.M.; Bhuiyan, M.S.; Karmakar, N.C.; Winther-Jensen, B. Development of a low cost printable chipless RFID humidity sensor. *IEEE Sens. J.* **2013**, *14*, 140–149. [[CrossRef](#)]
6. Feng, Y.; Xie, L.; Chen, Q.; Zheng, L.R. Low-cost printed chipless RFID humidity sensor tag for intelligent packaging. *IEEE Sens. J.* **2014**, *15*, 3201–3208. [[CrossRef](#)]
7. Delipinar, T.; Shafique, A.; Gohar, M.S.; Yapici, M.K. Fabrication and materials integration of flexible humidity sensors for emerging applications. *ACS Omega* **2021**, *6*, 8744–8753. [[CrossRef](#)]
8. Alrammouz, R.; Podlecki, J.; Abboud, P.; Sorli, B.; Habchi, R. A review on flexible gas sensors: From materials to devices. *Sens. Actuators A* **2018**, *284*, 209–231. [[CrossRef](#)]
9. Costa, J.C.; Spina, F.; Lugoda, P.; Garcia-Garcia, L.; Roggen, D.; Münzenrieder, N. Flexible sensors—From materials to applications. *Technologies* **2019**, *7*, 35. [[CrossRef](#)]
10. Kuzubasoglu, B.A. Recent studies on the humidity sensor: A mini review. *ACS Appl. Electron. Mater.* **2022**, *4*, 4797–4807. [[CrossRef](#)]
11. Su, P.G.; Shiu, W.L.; Tsai, M.S. Flexible humidity sensor based on Au nanoparticles/graphene oxide/thiolated silica sol-gel film. *Sens. Actuators B* **2015**, *216*, 467–475. [[CrossRef](#)]
12. Jeong, H.; Noh, Y.; Lee, D. Highly stable and sensitive resistive flexible humidity sensors by means of roll-to-roll printed electrodes and flower-like TiO<sub>2</sub> nanostructures. *Ceram. Int.* **2019**, *45*, 985–992. [[CrossRef](#)]
13. Najeeb, M.A.; Ahmad, Z.; Shakoor, R.A. Organic thin-film capacitive and resistive humidity sensors: A focus review. *Adv. Mater. Interfaces* **2018**, *5*, 1800969. [[CrossRef](#)]
14. Zhao, G.; Huang, Y.; Mei, C.; Zhai, S.; Xuan, Y.; Liu, Z.; Pan, M.; Rojas, O.J. Chiral nematic coatings based on cellulose nanocrystals as a multiplexing platform for humidity sensing and dual anticounterfeiting. *Small* **2021**, *17*, 2103936. [[CrossRef](#)]
15. Assunção da Silva, E.; Duc, C.; Redon, N.; Wojkiewicz, J. Humidity sensor based on PEO/PEDOT: PSS blends for breath monitoring. *Macromol. Mater. Eng.* **2021**, *306*, 2100489. [[CrossRef](#)]
16. Sobhanimatin, M.B.; Pourmahdian, S.; Tehranchi, M.M. Fast inverse opal humidity sensor based on acrylamide/AMPS hydrogel. *Mater. Today Commun.* **2021**, *26*, 101997. [[CrossRef](#)]
17. Zhang, Z.; Chen, M.; Alem, S.; Tao, Y.; Chu, T.-Y.; Xiao, G.; Ramful, C.; Griffin, R. Printed flexible capacitive humidity sensors for field application. *Sens. Actuators B* **2022**, *359*, 131620. [[CrossRef](#)]
18. Tekcin, M.; Sayar, E.; Yalcin, M.K.; Bahadir, S.K. Wearable and flexible humidity sensor integrated to disposable diapers for wetness monitoring and urinary incontinence. *Electronics* **2022**, *11*, 1025. [[CrossRef](#)]
19. Cheng, Y.; Xiong, Y.; Pan, M.; Li, L.; Dong, L. A flexible, sensitive and stable humidity sensor based on an all-polymer nanofiber film. *Mater. Lett.* **2023**, *330*, 133268. [[CrossRef](#)]
20. Li, X.; Chen, X.; Chen, X.; Ding, X.; Zhao, X. High-sensitive humidity sensor based on graphene oxide with evenly dispersed multiwalled carbon nanotubes. *Mater. Chem. Phys.* **2018**, *207*, 135–140. [[CrossRef](#)]
21. Wu, Y.; Huang, Q.; Nie, J.; Liang, J.; Joshi, N.; Hayasaka, T.; Zhao, S.; Zhang, M.; Wang, X.; Lin, L. All-carbon based flexible humidity sensor. *J. Nanosci. Nanotechnol.* **2019**, *19*, 5310–5316. [[CrossRef](#)] [[PubMed](#)]
22. Tulliani, J.M.; Insera, B.; Ziegler, D. Carbon-based materials for humidity sensing: A short review. *Micromachines* **2019**, *10*, 232. [[CrossRef](#)]
23. Liang, R.; Luo, A.; Zhang, Z.; Li, Z.; Han, C.; Wu, W. Research progress of graphene-based flexible humidity sensor. *Sensors* **2020**, *20*, 5601. [[CrossRef](#)]

24. Anichini, C.; Aliprandi, A.; Gali, S.M.; Liscio, F.; Morandi, V.; Minoia, A.; Beljonne, D.; Ciesielski, A.; Samorì, P. Ultrafast and highly sensitive chemically functionalized graphene oxide-based humidity sensors: Harnessing device performances via the supramolecular approach. *ACS Appl. Mater. Interfaces* **2020**, *12*, 44017–44025. [[CrossRef](#)] [[PubMed](#)]
25. Songkeaw, P.; Onlaor, K.; Thiawong, T.; Tunhoo, B. Transparent and flexible humidity sensor based on graphene oxide thin films prepared by electrostatic spray deposition technique. *J. Mater. Sci. Mater. Electron.* **2020**, *31*, 12206–12215. [[CrossRef](#)]
26. Hajian, S.; Zhang, X.; Khakbaz, P.; Tabatabaei, S.M.; Maddipatla, D.; Narakathu, B.B.; Blar, R.G.; Atashbar, M.Z. Development of a fluorinated graphene-based resistive humidity sensor. *IEEE Sens. J.* **2020**, *20*, 7517–7524. [[CrossRef](#)]
27. Gu, Y.; Jiang, H.; Ye, Z.; Sun, N.; Kuang, X.; Liu, W.; Li, G.; Song, X.; Zhang, L.; Bai, W. Impact of size on humidity sensing property of copper oxide nanoparticles. *Electron. Mater. Lett.* **2020**, *16*, 61–71. [[CrossRef](#)]
28. Li, P.; Yu, S.; Zhang, H. Preparation and performance analysis of Ag/ZnO humidity sensor. *Sensors* **2021**, *21*, 857. [[CrossRef](#)] [[PubMed](#)]
29. Nitta, R.; Lin, H.E.; Kubota, Y.; Kishi, T.; Yano, T.; Matsushita, N. CuO nanostructure-based flexible humidity sensors fabricated on PET substrates by spin-spray method. *Appl. Surf. Sci.* **2022**, *572*, 151352. [[CrossRef](#)]
30. Zhang, D.; Chang, H.; Li, P.; Liu, R.; Xue, Q. Fabrication and characterization of an ultrasensitive humidity sensor based on metal oxide/graphene hybrid nanocomposite. *Sens. Actuators B* **2016**, *225*, 233–240. [[CrossRef](#)]
31. Zhang, D.; Zong, X.; Wu, Z. Fabrication of tin disulfide/graphene oxide nanoflower on flexible substrate for ultrasensitive humidity sensing with ultralow hysteresis and good reversibility. *Sens. Actuators B* **2019**, *287*, 398–407. [[CrossRef](#)]
32. Zhang, D.; Xu, Z.; Yang, Z.; Song, X. High-performance flexible self-powered tin disulfide nanoflowers/reduced graphene oxide nanohybrid-based humidity sensor driven by triboelectric nanogenerator. *Nano Energy* **2020**, *67*, 104251. [[CrossRef](#)]
33. Chaloeipote, G.; Samarnwong, J.; Traiwatcharanon, P.; Kerdcharoen, T.; Wongchoosuk, C. High-performance resistive humidity sensor based on Ag nanoparticles decorated with graphene quantum dots. *R. Soc. Open Sci.* **2021**, *8*, 210407. [[CrossRef](#)] [[PubMed](#)]
34. Moustafa, H.; Morsy, M.; Ateia, M.A.; Abdel-Haleem, F.M. Ultrafast response humidity sensors based on polyvinyl chloride/graphene oxide nanocomposites for intelligent food packaging. *Sens. Actuators A* **2021**, *331*, 112918. [[CrossRef](#)]
35. Cai, C.; Zhao, W.; Yang, J.; Zhang, L. Sensitive and flexible humidity sensor based on sodium hyaluronate/MWCNTs composite film. *Cellulose* **2021**, *28*, 6361–6371. [[CrossRef](#)]
36. Singh, A.; Singh, P.K.; Mathuriya, A.S.; Sachdeva, A. Synthesis, characterisation and humidity sensing properties of PVA-NaI composite. *Mater. Today Proc.* **2022**, *49*, 3365–3369. [[CrossRef](#)]
37. Afnas, V.M.; Unnikrishnan, G.; Budhe, S.; Manaf, O.; Ameen, J. PVA/gelatin/chitin ternary blend as a humidity sensing material. *J. Mater. Sci. Mater. Electron.* **2022**, *33*, 2031–2043. [[CrossRef](#)]
38. Luo, M.; Liu, Z.; Wang, Q.; Liu, R.; Xu, Y.; Wang, K.; Shi, X.; Ye, S. Surface engineering on polyimide–silver films in low-cost, flexible humidity sensors. *ACS Appl. Mater. Interfaces* **2022**, *14*, 16621–16630. [[CrossRef](#)]
39. Kim, S.J.; Park, J.Y.; Lee, S.H.; Yi, S.H. Humidity sensors using porous silicon layer with mesa structure. *J. Phys. D Appl. Phys.* **2000**, *33*, 1781–1784. [[CrossRef](#)]
40. Fürjes, P.; Kovács, A.; Dücso, C.; Ádáma, M.; Müller, B.; Mescheder, U. Porous silicon-based humidity sensor with interdigital electrodes and internal heaters. *Sens. Actuators B* **2003**, *95*, 140–144. [[CrossRef](#)]
41. Harraz, F.A. Porous silicon chemical sensors and biosensors: A review. *Sens. Actuators B* **2014**, *202*, 897–912. [[CrossRef](#)]
42. He, X.W.; Geng, W.C.; Zhang, B.L.; Jia, L.M.; Duan, L.B.; Zhang, Q.Y. Ultrahigh humidity sensitivity of NaCl-added 3D mesoporous silica KIT-6 and its sensing mechanism. *RSC Adv.* **2016**, *6*, 38391–38398. [[CrossRef](#)]
43. Su, P.G.; Chen, I.C.; Wu, R.J. Use of poly(2-acrylamido-2-methylpropane sulfonate) modified with tetraethyl orthosilicate as sensing material for measurement of humidity. *Anal. Chim. Acta* **2001**, *449*, 103–109. [[CrossRef](#)]
44. Lv, X.; Li, Y.; Hong, L.; Luo, D.; Yang, M. A highly water-resistive humidity sensor based on silicon-containing polyelectrolytes prepared by one-pot method. *Sens. Actuators B* **2007**, *124*, 347–351. [[CrossRef](#)]
45. Zhao, H.; Zhang, T.; Dai, J.; Jiang, K.; Fei, T. Preparation of hydrophilic organic groups modified mesoporous silica materials and their humidity sensitive properties. *Sens. Actuators B* **2017**, *240*, 681–688. [[CrossRef](#)]
46. Zhao, H.; Zhang, T.; Qi, R.; Dai, J.; Liu, S.; Fei, T.; Lu, G. Organic-inorganic hybrid materials based on mesoporous silica derivatives for humidity sensing. *Sens. Actuators B* **2017**, *248*, 803–811. [[CrossRef](#)]
47. Qi, R.; Zhang, T.; Guan, X.; Dai, J.; Liu, S.; Zhao, H.; Fei, T. Capacitive humidity sensors based on mesoporous silica and poly(3,4-ethylenedioxythiophene) composites. *J. Colloid Interface Sci.* **2020**, *565*, 592–600. [[CrossRef](#)]
48. Su, P.G.; Huang, S.C. Electrical and humidity sensing properties of carbon nanotubes-SiO<sub>2</sub>-poly(2-acrylamido-2-methylpropane sulfonate) composite material. *Sens. Actuators B* **2006**, *113*, 142–149. [[CrossRef](#)]
49. Ma, M.; Li, H.; Xiong, Y.; Dong, F. Rational design, synthesis, and application of silica/graphene-based nanocomposite: A review. *Mater. Des.* **2021**, *198*, 109367. [[CrossRef](#)]
50. Zhu, J.; Zhang, N.; Yin, Y.; Xu, B.; Zhang, W.; Wang, C. High-sensitivity and low-hysteresis GO-NH<sub>2</sub>/mesoporous SiO<sub>2</sub> nanosphere-fabric-based humidity sensor for respiratory monitoring and noncontact sensing. *Adv. Mater. Interfaces* **2022**, *9*, 2101498. [[CrossRef](#)]
51. Zhang, J.; Zou, H.L.; Qing, Q.; Yang, Y.L.; Li, Q.W.; Liu, Z.F.; Quo, X.Y.; Du, Z.L. Effect of chemical oxidation on the structure of single-walled carbon nanotubes. *J. Phys. Chem. B* **2003**, *107*, 3712–3718. [[CrossRef](#)]

52. Casalbore-Miceli, G.; Yang, M.J.; Camaioni, N.; Mari, C.M.; Li, Y.; Sun, H.; Ling, M. Investigations on the ion transport mechanism in conduction polymer films. *Solid State Ion.* **2000**, *131*, 311–321. [[CrossRef](#)]
53. Wang, J.; Xu, B.K.; Ruan, S.P.; Wang, S.P. Preparation and electrical properties of humidity sensing films of BaTiO<sub>3</sub>/polystyrene sulfonic sodium. *Mater. Chem. Phys.* **2003**, *78*, 746–750. [[CrossRef](#)]

**Disclaimer/Publisher's Note:** The statements, opinions and data contained in all publications are solely those of the individual author(s) and contributor(s) and not of MDPI and/or the editor(s). MDPI and/or the editor(s) disclaim responsibility for any injury to people or property resulting from any ideas, methods, instructions or products referred to in the content.